Diffractive Efficiency Prediction of Surface Relief Grating Waveguide Using Artificial Neural Network

Fu-Li Hsiao, Hsuan-Ming Chang, Wen-Kai Lin, Ying-Pin Tsai*

Institute of Photonics, National Changhua University of Education, Changhua, Taiwan, ROC

Received 03 March 2024; received in revised form 15 April 2024; accepted 16 April 2024

DOI: https://doi.org/10.46604/ijeti.2024.13434

Abstract

This study aims to develop lightweight and comfortable wearable devices using surface-relief grating, which can be designed to meet different diffraction conditions. However, extensive calculations must be performed to obtain the impact of the variation in the structural dimensions. The finite element method is used to solve the diffractive efficiency and then replaced by trained artificial neural networks with a single hidden layer containing 25 neurons. By using raw data with geometric parameters as the features, the performance of the network is investigated with different numbers of raw data; in addition, the regression analysis shows a high R-value of approximately 0.999. The predicted results are compared with those calculated from the simulation. The diffraction efficiency tendencies vary with the different geometric parameters, which show a high level of agreement between the predicted and calculated data; this confirms that the proposed method supports and reduces the burden of extensive calculations.

Keywords: surface relief grating, diffractive efficiency, finite element method, artificial neural network

1. Introduction

Due to the flourishing development of virtual reality (VR), augmented reality (AR) [1], and mixed reality (MR) [2], the research and optimization of head-mounted displays (HMDs) have become crucial in recent years [3-6]. To enhance the ease with which people can enter the virtual world, a lightweight design has become key to the creation of HMDs, serving as an interface between the real and virtual worlds and enabling them to be worn for an extended period. In traditional display systems, the light of the image is directed from a projector to a display through diverse combiner configurations with multiple optical components. Such structures not only require a larger space to accommodate multiple elements but also increase the overall weight; this significantly affects the comfort and portability of the device during extended usage. Moreover, the system is constrained by the design of the combiner, which significantly affects its flexibility.

The use of waveguide-guided optical systems has emerged as a popular solution in recent years [7-13]. Since Levola [10] proposed building VR displays using the diffractive waveguide in 2006, numerous studies on this technology have been conducted. The coupling of light into the waveguide is another aspect that requires consideration. The volume of the system can be reduced by fabricating diffractive optical elements on the waveguide surface to efficiently couple incident information light. This methodology has enabled the design of diffraction elements that are tailored to different input conditions. Different diffractive optical elements, such as surface-relief gratings (SRGs), volume holographic gratings, and meta-surfaces, are employed as in-couplers or out-couplers to concentrate energy into specific diffraction orders.

* Corresponding author. E-mail address: yingpintsai@gmail.com

English language proofreader: Chih-Wen Teng

To take full advantage of the information light, a polarization–multiplexing meta-grating was proposed in 2021 by Liu et al. [11]. The incident circularly polarized light can be separated into opposite diffraction orders by the specially designed phase-based meta-grating according to the different handedness. This approach, which involves information light directly carrying two stereoscopic images with opposite circular polarization, enables 3D vision. On the other hand, Lin et al. [12] optimized the diffraction efficiency by inserting an interlayer into a traditional diffractive waveguide. The potential use of several optical materials as the inserting layer was discussed in this study, with MgF_2 finally being selected as the inserting material. Via the insertion layer, the proposed diffractive waveguide can enhance the optical efficiency of the waveguide and produce an angular selectivity. In 2023, Liu et al. [13] proposed a programable on-chip integrated metasystem that can produce a wavelength-demultiplexing projection of an image.

The in-coupler is inverse-designed to fit two different wavelengths in the visible light range and can diffract them into different directions. After being manipulated by these diffractive elements, the image enters the waveguide, propagates through total internal reflection (TIR), and is directed toward the emitting position. The light exits the waveguide through a coupler featuring the same diffraction conditions and is guided to the observer's eyes [14]. SRG is a design commonly used for diffractive optical elements [15-23]. Via the direct fabrication of grating structures on the surface of the waveguide, various SRG structures have been proposed to achieve a high diffraction efficiency. Typically, SRGs consist of groove-shaped structures on the surface, with an additional slanted angle applied on the grooves; the diffractive light can therefore be concentrated into first-order diffractions. To further enhance the diffraction efficiency, SRG structures with different shapes have been designed; these include blazed grating [20], trapezoidal grating [21], 2D SRG [22], or even double-layer grating [23], thus increasing the complexity of SRGs.

To concentrate the diffractive energy on the first-order diffraction while suppressing the zero-order diffraction, a non-symmetry shape is frequently required for SRG structures; for example, grooves with inclined angles can be used. The SRG's non-symmetric periodic structure makes it sensitive to the incident angle and wavelength of the incoming light, with a narrow range of incident angles and wavelengths leading to the realization of a high diffraction efficiency. Diffractive optical elements based on the SRG design are therefore able to achieve low dispersion and a wide field of view in an image display. Although display elements that are designed based on SRGs suppress zero-order diffraction, if the -1-order and +1-order diffractions have comparable efficiencies, a partial loss of energy will be observed. For HMDs, this allows observers other than the user to see the displayed content, thus infringing on the user's privacy and security.

To perform an optimization analysis on the designed SRG components, the geometric parameters of the structure are treated as variables and their efficiency at ±1-order diffraction is determined by the number of calculations. In addition to providing the optimal structure size with the highest efficiency, this enables tables based on different incident angles to be generated; these reference tables for different sizes can then be searched for the best diffraction efficiency or diffraction angle at the corresponding incident angle. Compared to the rigorous coupled-wave analysis (RCWA) that is frequently used in traditional calculations, this study uses the finite element method (FEM) [24], which is suitable for problems with higher levels of complexity.

Based on the calculation method that meshes whole structures into small elements, the FEM is well-known for its ability to solve physical problems in complex structures or those with multiple physical conditions; it can also simultaneously account for multiple variables, such as different incident angles with different incident wavelengths. Despite its ability to handle complex calculations more efficiently, this analysis process still requires a significant amount of time. If detailed size–efficiency relationships must be calculated using reference tables, the computational workload will increase.

In recent years, artificial neural networks (ANNs) have been used to solve repetitive problems with complex relations that must be calculated. This extraordinary capacity for calculation has been used to design optical devices [25-28]. To achieve the inverse design of optical elements, the tandem network training needs a forward modeling network to confirm the accuracy of

the inverse-prediction component; therefore, a forward prediction network is necessary [28]. This study uses ANNs to assist in calculating the diffraction efficiency of SRG components. Two separate ANNs are trained based on the diffraction efficiency of the +1-order and the -1-order diffraction; this enables calculations to be performed with high efficiency when using the geometric parameters and the incident angle as the input data. This study also examines the impact of using various amounts of data in the ANN training datasets to reduce the computational workload required. Finally, this study shows the actual results obtained by the ANN when inputting data that are not included in the training dataset.

2. Materials and Methods

Fig. 1 shows a unit cell of the SRG, which is created by arranging periodically slanted grooves on a glass waveguide surface that has refractive indices of 1.5 and 1 for the glass and air, respectively. The incident light comes from the air below, which has a wavelength of 532 nm, and is transmitted into the glass waveguide.

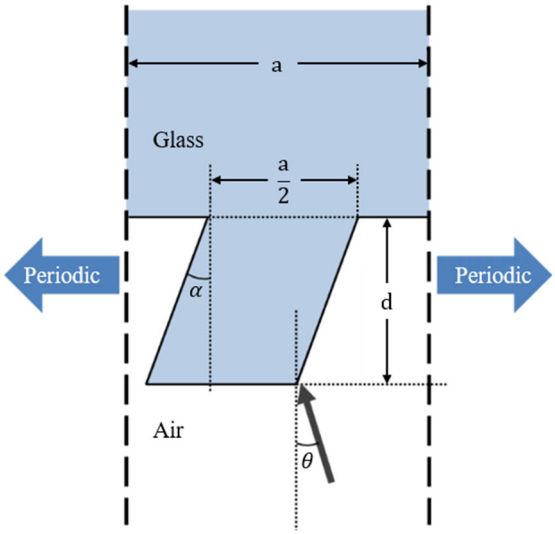

Fig. 1 Sketch of the unit cell of the SRG

In the figure, the period length is a = 433 nm, and the groove width is set as half of a. The groove depth is defined as d, and the slant angle is defined as α. External incident light enters from the air below and is set by a port boundary condition, with the incident angle defined as θ. Another port boundary condition is applied to the top boundary of the unit cell within the glass waveguide, and the receiver receives the transmitted light and calculates the diffraction efficiency. By setting periodic boundary conditions on both sides of the unit cell, the FEM can simulate the infinite periodic grating structure within the unit cell and compute the corresponding diffraction efficiency. The incoming light comes from the area of air below and is transmitted into the SRG made of glass in the above area. The periodic boundary conditions are applied to the boundaries on both sides of the unit cell.

In the FEM setup, both incident and diffracted light travel through the port interfaces, and S-parameter calculations are used to determine the efficiency of different diffraction orders. As the main variables, the depth d is calculated from 50 nm to 500 nm, and owing to fabrication constraints, the slant angle α is only considered from 0° to 20°. Considering the influence that light incidence from different directions has on the structure, the slant angle is fixed at a positive value, and the incident angle θ is considered from -10° to 10°. The values of α and θ, which are labeled in the figure, are positive and are counted from the normal line. Several components can be obtained under different diffraction conditions by varying the three variables mentioned above. The ±1-order diffraction results and diffraction efficiencies for each component are calculated using the FEM. The obtained data serve as the original database, from which several data are extracted for the subsequent training of the ANN. The data not used for training can be employed as test data to evaluate the ability of the trained ANN to predict the diffraction efficiency.

The ANN configuration used to predict the diffraction efficiency is shown in Fig. 2. The figure shows that the ANN has a simple basic structure that consists of three main layers: the input, hidden, and output layers. In the input layer, three parameters — the geometric parameters d, α, and the incident angle θ — serve as the input features and are fed into the training dataset through three neurons. To use the ANN to replace extensive computations at its full capacity, not all the data solved by the FEM are used in the training dataset.

In this study, the slant angle α is sampled every 4°, totaling six values, and the incident angle θ is sampled every 5°, totaling five values for the training data. Finally, owing to its broad coverage, the depth d is divided into three groups for comparison, and each is sampled at 20, 30, and 50 nm. Therefore, each group of datasets contains six slant angle α values and five incident angle θ values with different depth d values for the training of the ANN. Subsequently, the influence that the amount of training data used has on the training results is compared.

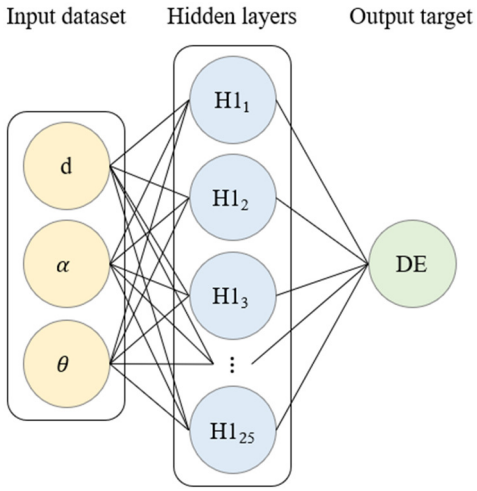

Fig. 2 ANN configuration for diffractive efficiency prediction

The geometric parameters d and α, as well as the incident angle θ, are input as the training features; the +1-order and the -1-order diffraction efficiencies are, respectively, treated as the training target in the output layer. In the hidden layer, the number of hidden layers and neurons within each layer are considered variables. However, in this study, the variation in the diffraction efficiency is more linear compared to other problems, and some of the calculations have explicit formulas. Therefore, in this study, a simple single-layer hidden layer structure is used, and only 25 neurons are required to provide sufficient fitting. Finally, to provide different diffraction efficiencies based on the different conditions in which the diffraction element is used, the diffraction efficiencies of the ±1-order diffractions are predicted separately using two ANNs. In the output layer, the +1-order and the -1-order diffraction efficiencies are used as the training target for the two ANNs, and a single output neuron is used in the output layer for both ANNs. These predicted values are then compared with the diffraction efficiencies calculated using the FEM.

3. Results

Figs. 3-4 shows the regression analysis results of the two networks used to predict the +1-order and the -1-order diffractions. The networks are trained using datasets that contain varying amounts of data. The regression analysis plots the target values of the neural network on the horizontal axis and the actual values obtained by the ANN on the vertical axis, with each result predicted for each input data point plotted on a graph. When the predicted values are closer to the target values, the data points are closer to the diagonal line x = y. Therefore, when the slope of the linear regression results for all the data points is closer to 1, the predicted results are more accurate. Figs. 3(a) to 3(c) shows the training results for the +1-order diffraction. They are presented sequentially, with one sample taken every 20, 30, and 50 nm for depth d; these are extracted from the original database, totaling 690, 480, and 300 training data points, respectively.

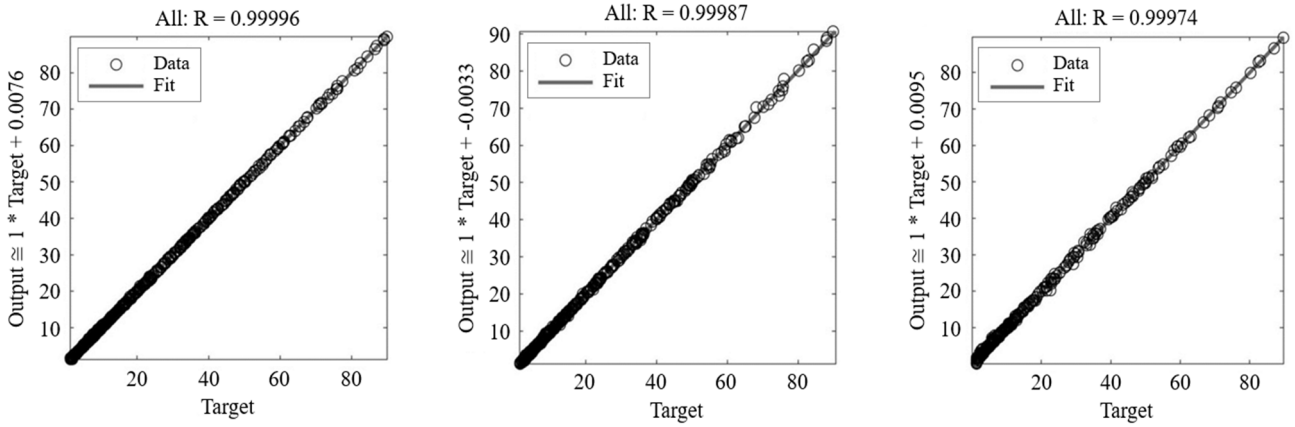

(a) Depth d took every 20 nm (b) Depth d took every 30 nm (c) Depth d took every 50 nm

Fig. 3 Regression analysis for +1-order diffraction efficiency with different quantities of depth d data

According to the R-values shown at the top of each graph in Figs. 3-4, as the quantity of extracted data decreases, the regression coefficient R also decreases. However, even when less than half of the originally available data shown in Fig. 3(c) is used, a high R-value exceeding 0.999 is maintained. On the contrary, Figs. 4(d) to 4(f) shows the training results obtained for the -1-order diffraction. Similar to the +1-order diffraction, it is evident that as the quantity of sampled data decreases, the R-value decreases. Although the R-value in Fig. 3(f) decreases below 0.999, indicating a slight decrease in accuracy, it remains within an acceptable range.

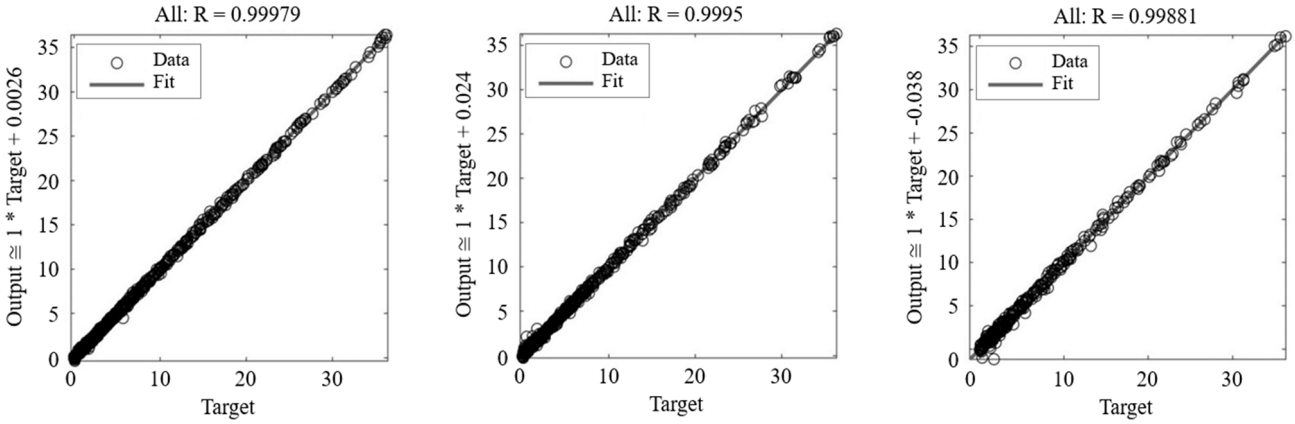

(a) Depth d took every 20 nm (b) Depth d took every 30 nm (c) Depth d took every 50 nm

Fig. 4 Regression analysis for -1-order diffraction efficiency with different quantities of depth d data

The diffraction efficiency results produced by the ANN when using minimal training data and those obtained by the FEM were compared, as shown in Fig. 5. Because this study involves the simultaneous use of three variables, Fig. 5 plots the diffraction efficiency using each variable on the x-axis while appropriately selecting values for the remaining two variables; this is for ease of comparison. Figs. 5(a) to 5(c) shows the trends in the diffraction efficiency as the corresponding parameter varies. First, Fig. 5(a) shows the variation in the +1-order diffraction efficiency as α varies. The lines represent the trends obtained using the FEM calculations, and the markers represent the predicted results generated by the ANN.

The results for the two sets of parameter combinations are plotted separately in the figure. In this context, Sim. and Pre. (Case 1) represent the results for d = 350 nm and θ = -10°, while Sim. and Pre. (Case 2) represent the results for d = 350 nm and θ = 10°. Thus, from Fig. 5(a), it can be observed that for +1-order diffraction under the conditions of $\alpha > 0$, θ = 10° is required to achieve high +1-order diffraction efficiency. Furthermore, under the condition of θ = 10°, α of approximately 18° provides the highest +1-order diffraction efficiency, reaching approximately 50%. A comparison between the results predicted by the ANN and the FEM calculations revealed that they were in almost perfect accord with the actual calculated values. The markers

in the figure represent the data extracted every 2°; in contrast to the sampling in which α is extracted every 4°, it can be observed that some of the data points not included in the training dataset are interspersed and still provide continuous and accurate predictions.

Subsequently, in Fig. 5(b), with θ as the horizontal axis, the variations in the +1-order diffraction efficiency are shown for two SRG structures with d = 350 nm and α = 4° and 14°. The results are depicted by Sim. and Pre. (Case 1) for α = 4° and Sim. and Pre. (Case 2) for α = 14°. Since α is sampled every 4°, α = 14° is not included in the training dataset, indicating that this set of data belongs to the test data. In the figure, it can be observed that when the groove slant angle is 14°, the +1-order diffraction efficiency has a maximum value of approximately 65% at an incident angle of positive 5°. When the slant angle is small, the highest first-order diffraction efficiency occurs at an incident angle of 10°.

When comparing the results of the ANN and FEM, it is evident that even the data for α = 14°, which was not included in the training dataset, shows good fitting. The overall maximum error occurred in the data for α = 4°, as indicated by the marked point in the figure, with a numerical error of approximately 1.55. Finally, for the first-order diffraction results, Fig. 5(c) shows d on the horizontal axis. The Sim. and Pre. (Case 1) represent the results for α = 4° and θ = 10°, while the Sim. and Pre. (Case 2) represent the results for α = 14° and θ = 10°. It can be observed that the structure represented by the Sim. and Pre. (Case 2) exhibited a significantly high +1-order diffraction efficiency and reached its maximum at approximately d = 380 nm. Regarding the performance of the ANN predictions, both structures exhibited excellent fitting results, with slight errors in the range of d = 300–350 nm.

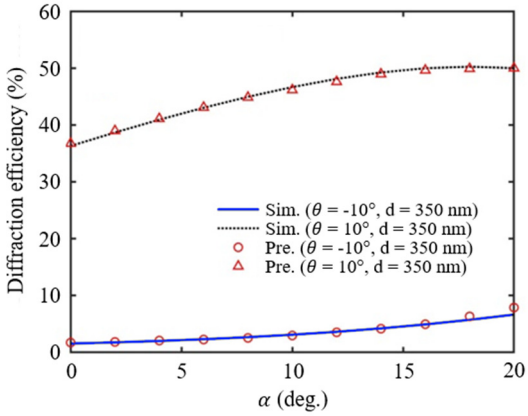

(a) Efficiency varies with α

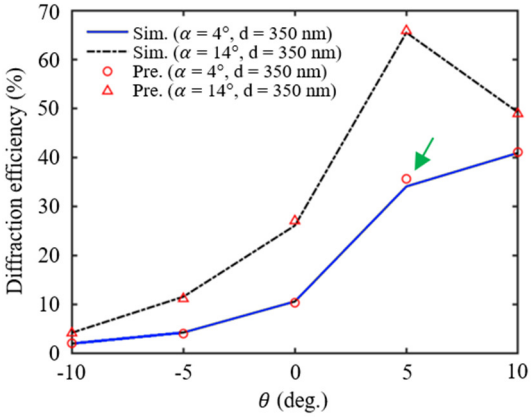

(b) Efficiency varies with θ

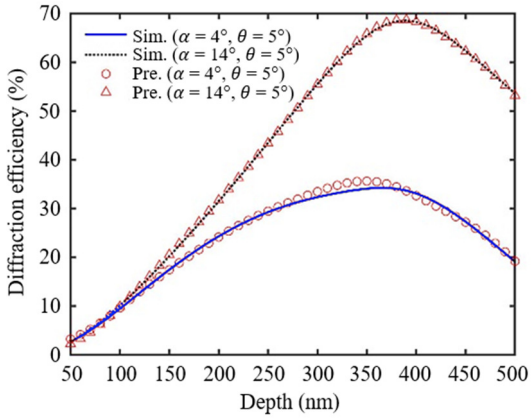

(c) Efficiency varies with d

Fig. 5 +1-order diffraction efficiencies at 50 nm with varying parameters

On the other hand, Fig. 6 compares the results of the -1-order diffraction efficiencies predicted by the ANN and the results calculated by the FEM. Fig. 6 uses α, θ, and d as the horizontal axes, respectively, to present the corresponding -1-order diffraction efficiency, as is the case in Fig. 5. First, it can be observed from all three figures that, compared to the +1-order

diffraction efficiency, the -1-order diffraction efficiency was effectively suppressed at lower levels, showing an inversely proportional trend between the +1-order and -1-order diffraction. Regarding the ANN predictions, it can be observed from Fig. 6(a) and 6(b) that Pre. (Case 1) and Pre. (Case 2) overlap significantly with the line graph of the FEM calculations, indicating that the ANN exhibits a high level of accuracy. In Fig. 6(c), there is more error around d = 300–350 nm, which suggests that this part of the data has a higher level of similarity in the raw database; this makes it challenging to distinguish and predict the precise values. Simultaneously, the maximum value on the y-axis in Fig. 6(c) is 8%, indicating that even though there appears to be a larger error in this figure, the actual numerical difference is less than 0.5.

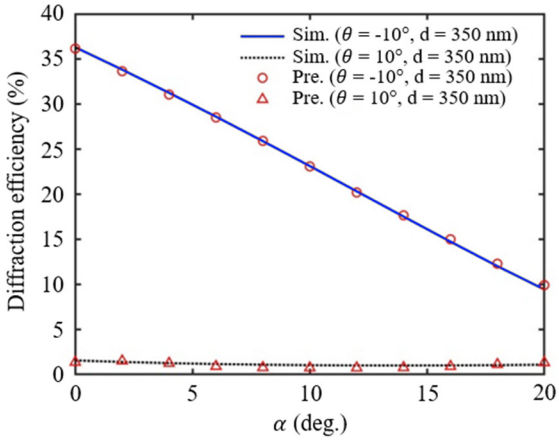

(a) Efficiency varies with α

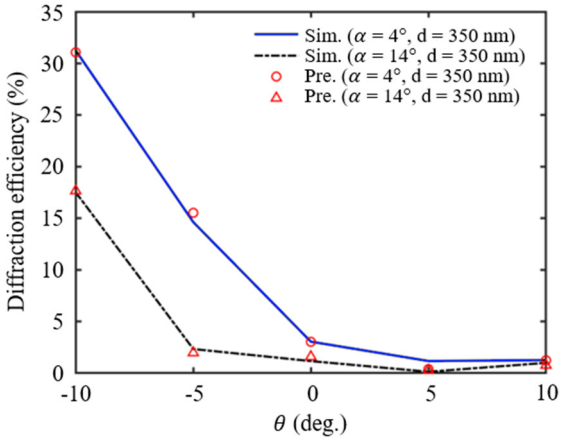

(b) Efficiency varies with θ

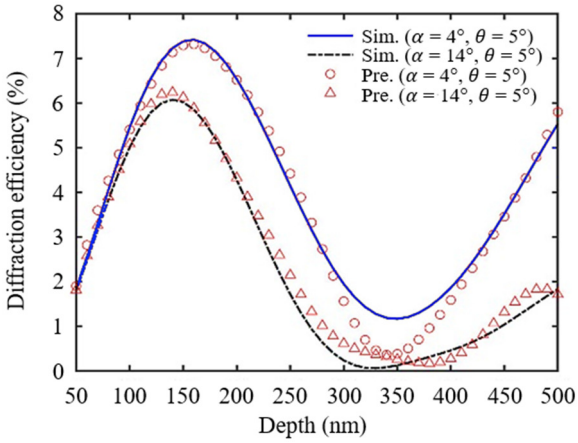

(c) Efficiency varies with d

Fig. 6 -1-order diffraction efficiencies at 50 nm with identical parameters

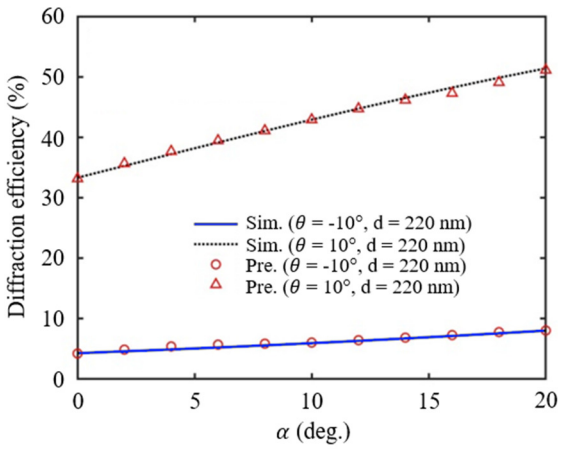

(a) +1-order efficiency variation with α

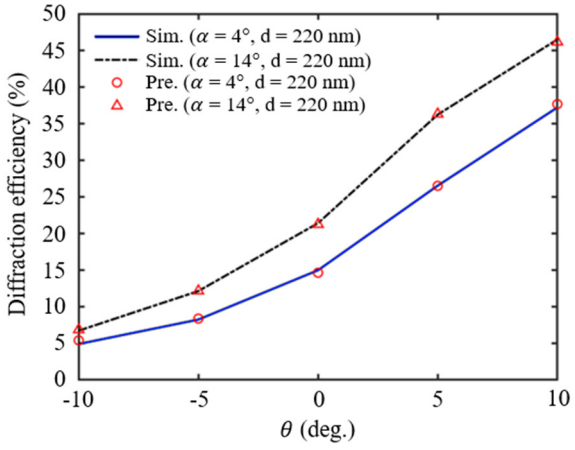

(b) +1-order efficiency variation with θ

Fig. 7 Predicted efficiencies for a d = 220 nm SRG using ANN with a 50 nm training sample

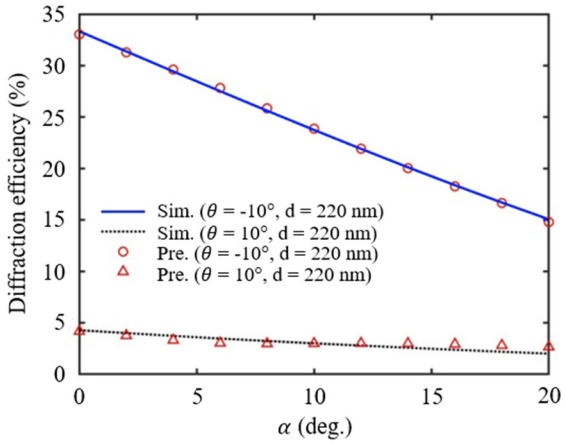

(c) -1-order efficiency variation with α

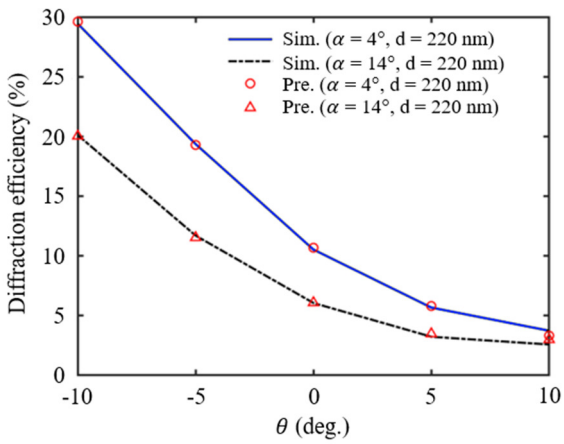

(d) -1-order efficiency variation with θ

Fig. 7 Predicted efficiencies for a d = 220 nm SRG using ANN with a 50 nm training sample (continued)

Finally, to test the predictive performance of the ANN using non-training set data, the diffraction efficiency lines corresponding to d = 220 nm, which is not included in the training dataset, are drawn in Fig. 7; this is similar to using $\alpha = 14°$ in Figs. 5-6. Figs. 7(a) and 7(b) show the +1-order diffraction efficiencies corresponding to Figs. 5(a) and 5(b), respectively. Figs. 7(c) and 7(d) represent the -1-order diffraction efficiencies corresponding to Figs. 6(d) and 6(e). As shown in Fig. 7, the ANN prediction results marked with red circles and red triangles overlap significantly with the lines calculated using the FEM. In Fig. 7(c), there is a slight deviation in some of the Pre. (Case 2) points on the Sim. (Case 2) line representing $\theta = 10°$, but it still maintains an error below 1%.

4. Discussion

According to the regression analysis in Fig. 3, it can be concluded that an ANN configuration with a single hidden layer containing 25 neurons can accurately predict the diffraction efficiency. Moreover, only 300 training data points were required to achieve an accuracy close to 0.999, thus effectively reducing the preparation time required for ANN training and the computation time required for SRG research. By comparing the predicted results obtained by the ANN with the values calculated by the FEM, it can be confirmed that almost all the structural parameters yielded results that did not differ significantly from the numerical calculations.

In this study, because the SRG was designed to concentrate the diffraction efficiency on +1-order diffraction, the evident suppression of the -1-order diffraction led to smaller numerical differences between the target values. Consequently, when the same weight was applied to predict most of the other values associated with the -1-order diffraction, it was challenging for the ANN to predict small values with small differences accurately. This challenge was reflected in a decrease in the overall accuracy, as shown in the results in Fig. 6(f). However, the error remained within a relatively small range and did not significantly affect the primary outcomes. Finally, based on the results in Figs. 4-7, it is evident that the ANN could accurately predict the diffraction efficiency, even for test data that were not included in the training dataset; the objective of replacing numerical calculations was therefore achieved.

5. Conclusion

In this study, the proposed method uses a relatively simple ANN architecture that requires only a small amount of training data to directly predict the ±1-order diffraction efficiencies of the corresponding diffractive devices based on their structural dimensions and incident angles. Considering the inherent linear relationship in the diffraction efficiency of the SRG components, the amount of training data required could be further reduced by increasing the number of hidden layers or

neurons in the hidden layers of the ANN architecture. This reduction in the time required to prepare the data could potentially enhance the capabilities of auxiliary calculations. The proposed method could be further developed into an inverse design network, as the forward training process.

Conflicts of Interest

The authors declare no conflict of interest.

References

[1] R. T. Azuma, "A Survey of Augmented Reality," Presence: Teleoperators and Virtual Environments, vol. 6, no. 4, pp. 355-385, August 1997.

[2] S. Rokhsaritalemi, A. Sadeghi-Niaraki, and S. M. Choi, "A Review on Mixed Reality: Current Trends, Challenges and Prospects," Applied Sciences, vol. 10, no. 2, article no. 636, January 2020.

[3] D. Cheng, Q. Wang, Y. Liu, H. Chen, D. Ni, X. Wang, et al., "Design and Manufacture AR Head-Mounted Displays: A Review and Outlook," Light: Advanced Manufacturing, vol. 2, no. 3, pp. 350-369, 2021.

[4] C. W. Pansing, H. Hua, and J. P. Rolland, "Optimization of Illumination Schemes in a Head-Mounted Display Integrated with Eye Tracking Capabilities," Novel Optical Systems Design and Optimization VIII, vol. 5875, pp. 128-140, August 2005.

[5] X. Sang, Z. Chen, X. Gao, B. Yan, H. Li, Y. Wang, et al., "Design and Fabrication of a Wide-Angle Off-Axis Three-Mirror Head-Mounted Display System," Optik, vol. 191, pp. 139-145, August 2019.

[6] T. Shibata, "Head Mounted Display," Displays, vol. 23, no. 1-2, pp. 57-64, April 2002.

[7] E. DeHoog, J. Holmstedt, and T. Aye, "Field of View Limitations in See-Through HMDs Using Geometric Waveguides," Applied Optics, vol. 55, no. 22, pp. 5924-5930, August 2016.

[8] J. A. Piao, G. Li, M. L. Piao, and N. Kim, "Full Color Holographic Optical Element Fabrication for Waveguide-Type Head Mounted Display Using Photopolymer," Journal of the Optical Society of Korea, vol. 17, no. 3, pp. 242-248, June 2013.

[9] M. L. Piao and N. Kim, "Achieving High Levels of Color Uniformity and Optical Efficiency for a Wedge-Shaped Waveguide Head-Mounted Display Using a Photopolymer," Applied Optics, vol. 53, no. 10, pp. 2180-2186, April 2014.

[10] T. Levola, "Diffractive Optics for Virtual Reality Displays," Journal of the Society for Information Display, vol. 14, no. 5, pp. 467-475, May 2006.

[11] Z. Liu, C. Zhang, W. Zhu, Z. Huang, H. J. Lezec, A. Agrawal, et al., "Compact Stereo Waveguide Display Based on a Unidirectional Polarization-Multiplexed Metagrating In-Coupler," ACS Photonics, vol. 8, no. 4, pp. 1112-1119, April 2021.

[12] Y. Lin, H. Xu, R. Shi, L. Lu, S. T. Zhang, and D. Li, "Enhanced Diffraction Efficiency with Angular Selectivity by Inserting an Optical Interlayer into a Diffractive Waveguide for Augmented Reality Displays," Optics Express, vol. 30, no. 17, pp. 31244-31255, August 2022.

[13] Y. Liu, Y. Shi, Z. Wang, and Z. Li, "On-Chip Integrated Metasystem with Inverse-Design Wavelength Demultiplexing for Augmented Reality," ACS Photonics, vol. 10, no. 5, pp. 1268-1274, May 2023.

[14] L. Eisen, M. Meyklyar, M. Golub, A. A. Friesem, I. Gurwich, and V. Weiss, "Planar Configuration for Image Projection," Applied Optics, vol. 45, no. 17, pp. 4005-4011, June 2006.

[15] S. K. Bag, M. Wan, R. K. Sinha, and S. K. Varshney, "Design and Characterization of Surface Relief Grating on Etched Multimode Optical Fiber for Refractive Index Sensing," Sensors and Actuators A: Physical, vol. 303, article no. 111836, March 2020.

[16] J. S. Maikisch and T. K. Gaylord, "Optimum Parallel-Face Slanted Surface-Relief Gratings," Applied Optics, vol. 46, no. 18, pp. 3674-3681, June 2007.

[17] J. M. Miller, N. de Beaucoudrey, P. Chavel, J. Turunen, and E. Cambril, "Design and Fabrication of Binary Slanted Surface-Relief Gratings for a Planar Optical Interconnection," Applied Optics, vol. 36, no. 23, pp. 5717-5727, August 1997.

[18] P. Karpinski and A. Miniewicz, "Surface Plasmon Polariton Excitation in Metallic Layer via Surface Relief Gratings in Photoactive Polymer Studied by the Finite-Difference Time-Domain Method," Plasmonics, vol. 6, no. 3, pp. 541-546, September 2011.

[19] F. Reda, M. Salvatore, F. Borbone, P. Maddalena, and S. L. Oscurato, "Accurate Morphology-Related Diffraction Behavior of Light-Induced Surface Relief Gratings on Azopolymers," ACS Materials Letters, vol. 4, no. 5, pp. 953-959, May 2022.

[20] J. Gao, P. Chen, L. Wu, B. Yu, and L. Qian, "A Review on Fabrication of Blazed Gratings," Journal of Physics D: Applied Physics, vol. 54, no. 31, article no. 313001, August 2021.

[21] T. Levola and P. Laakkonen, "Replicated Slanted Gratings with a High Refractive Index Material for In and Outcoupling of Light," Optics Express, vol. 15, no. 5, pp. 2067-2074, March 2007.

[22] S. Nair, C. Escobedo, and R. G. Sabat, "Crossed Surface Relief Gratings as Nanoplasmonic Biosensors," ACS Sensors, vol. 2, no. 3, pp. 379-385, March 2017.

[23] W. C. Liu, G. Jin, Y. F. Xie, P. Sun, B. Zhou, W. Jia, et al., "Broadband High-Efficiency Polarization-Independent Double-Layer Slanted Grating for RGB Colors," Optics Communications, vol. 488, article no. 126864, June 2021.

[24] M. R. Seba and S. Kebdani, "Finite Element and Neural Network Based Predictive Model to Determine Natural Frequency of Laminated Composite Plates with Eccentric Cutouts Under Free Vibration," Advances in Technology Innovation, vol. 7, no. 2, pp. 131-142, April 2022.

[25] T. Asano and S. Noda, "Optimization of Photonic Crystal Nanocavities Based on Deep Learning," Optics Express, vol. 26, no. 25, pp. 32704-32717, December 2018.

[26] T. Asano and S. Noda, "Iterative Optimization of Photonic Crystal Nanocavity Designs by Using Deep Neural Networks," Nanophotonics, vol. 8, no. 12, pp. 2243-2256, December 2019.

[27] R. Li, X. Gu, K. Li, Y. Huang, Z. Li, and Z. Zhang, "Deep Learning-Based Modeling of Photonic Crystal Nanocavities," Optical Materials Express, vol. 11, no. 7, pp. 2122-2133, July 2021.

[28] D. Liu, Y. Tan, E. Khoram, and Z. Yu, "Training Deep Neural Networks for the Inverse Design of Nanophotonic Structures," ACS Photonics, vol. 5, no. 4, pp. 1365-1369, April 2018.